Influence of preparation methods of LaCoO$_3$ on the catalytic performances in the decomposition of N$_2$O

J.P. Dacquin [a], C. Lancelot [a], C. Dujardin [a,*], P. Da Costa [b], G. Djega-Mariadassou [b], P. Beaunier [b], S. Kaliaguine [c], S. Vaudreuil [c], S. Royer [d], P. Granger [a]

[a] Unité de Catalyse et de Chimie de Solide, UMR 8181, Université des Sciences et Technologies de Lille, Bâtiment C3, 59655 – Villeneuve d'Ascq, France
[b] Laboratoire de Réactivité de Surface, UMR 7197, 4, place Jussieu - Tour 54-55, 75252 Paris, France
[c] Département de génie chimique, Université Laval, Sainte Foy, Québec, G1K7P4 Canada
[d] Laboratoire de Catalyse en Chimie Organique, UMR 6503, 40 Av. du Recteur Pineau, 86022 Poitiers, France

ARTICLE INFO

ABSTRACT

This study reports the potential interest of LaCoO$_3$ in the catalytic decomposition of N$_2$O from nitric acid plants. Typically, the exhaust gas contains NO, water and O$_2$ which usually induce strong inhibiting effects depending on the surface properties of the solids particularly the surface mobility of oxygen from LaCoO$_3$. Different preparation methods have been implemented, involving citrate route, reactive grinding and the use of templates, which lead to different structural and textural properties examined by X-ray diffraction, transmission electron microscopy and N$_2$ physisorption. EDX analysis and XPS measurements also revealed that different surface composition may alter subsequent interactions between the surface and the reactants and related catalytic performances. LaCoO$_3$ prepared by reactive grinding was found to be the most active catalyst due to a high specific surface area but the presence of Fe and Zn impurities inherent to the preparation method were suggested to interfere on the catalytic performances.

© 2009 Elsevier B.V. All rights reserved.

1. Introduction

A wide number of publications deals with the implementation of catalytic processes for the removal of NO$_x$ from mobile and stationary sources. On the other hand, only a few of them concerns nitrous oxide (N$_2$O) which exhibits a greenhouse gas behavior with a global warming power of approximately 300 higher than that of CO$_2$ [1–7]. Perovskite-based catalysts (ABO$_3$) can be attractive due to their lower cost and the flexibility of their composition because they can tolerate significant substitution and non-stoichiometry [8]. These peculiar properties have been previously developed for the direct catalytic decomposition of NO into N$_2$ and O$_2$ [9–13] and could be profitably used for the decomposition of N$_2$O. Such a technology is simple and economically attractive without any supply of reducing agents. On the other hand, it usually suffers from deactivation phenomena due to strong oxygen adsorption.

Modified perovskite-based catalysts, with incorporation of noble metals, have also been investigated as three-way catalysts [14] and/or under lean conditions [15–17]. In those typical conditions, the usual oxygen-inhibiting effect and related surface

processes are attenuated. Nevertheless, earlier studies also revealed that those materials are sensitive to the presence of CO$_2$ and water which may considerably alter their surface properties [18]. Hence, in the typical exhaust gas composition from nitric acid plants containing N$_2$O, NO$_x$, oxygen and water, the rate of N$_2$O decomposition can be altered due to competitive adsorptions of those different molecules [19]. On the basis of those considerations, it is expected that the physicochemical properties of the solid, particularly the mobility of oxygen species, may determine the intrinsic catalytic performances. Earlier comparative studies emphasized the fact that the experimental method implemented for the preparation of those solids strongly influences the catalytic performances. Generally, the main drawback is associated to the involvement of high temperature to ensure the structural properties of perovskites which induces a significant loss of specific surface area. Today, significant improvements have been achieved on the synthesis of those solids with the development of sol–gel methods using citrate as complexing agent [20] and more recently innovative nanotechnological approaches which lead to significant gain on the textural properties [21,22]. Alternative methods have also been developed by Szabo et al. [23] using a technique designated as reactive grinding for the synthesis of LaCo$_{1−x}$Fe$_x$O$_3$ in VOC oxidation. Comparable perovskite structures [24] were synthesized at room

* Corresponding author. Tel.: +33 3 28 77 85 29; fax: +33 3 20 43 65 61.
E-mail address: christophe.dujardin@univ-lille1.fr (C. Dujardin).

temperature according to this procedure involving high-energy ball milling. This paper reports a comparative investigation of the catalytic performances of LaCoO$_3$ in the decomposition of N$_2$O. Different synthesis routes via sol–gel, template and reactive grinding approaches have been implemented and compared. Correlations between physicochemical characterization and catalytic properties have been tentatively established and showed that structural and textural properties do not completely govern the catalytic performances.

2. Experimental

2.1. Catalyst preparation

LaCoO$_3$ was prepared according to different experimental protocols earlier described [20,22–26]. A so-called sol–gel method (SG) was implemented according to a conventional citrate route. Cobalt and lanthanum nitrate salts were dissolved in the presence of citric acid (AC) according to the molar AC/(Co + La) ratio equal to 1. The solvent was removed by heating at 60 °C under vacuum until the formation of a gel. After drying at 80 °C, nitrates were decomposed at 200 °C before calcination in air at 600 °C for 8 h. The solid thus obtained was labelled LaCoO$_3$(SG). The colloidal crystal templating method LaCoO$_3$(T) involved preliminary dissolution of cobalt and lanthanum nitrate precursor salts into a solution containing ethylene glycol and methanol. Polystyrene spheres [27] (diameter $\cong$ 400 nm) were introduced in order to form a colloidal network where the solution can penetrate. According to the high viscosity of the solution the contact between the solution and the polystyrene spheres was maintained for 5 h. Subsequent filtration, drying overnight at 80 °C and calcination in air at 600 °C led to LaCoO$_3$(T). Finally, LaCoO$_3$(RG) prepared by reactive grinding involved a two-step process as described elsewhere [23,24]. Co$_3$O$_4$ and La$_2$O$_3$ were preliminary calcined at 600 °C. Then, the solids were crushed at room temperature under O$_2$ at 1000 rpm in order to obtain the perovskite structure containing residual Co$_3$O$_4$ and La$_2$O$_3$ impurities and exhibiting a low specific surface area ($\cong$ 10 m^2/g). The milling proceeded at room temperature using steel vial and balls. A second step of grinding was done in the presence of additives (ZnO) in order to increase the specific surface area. Finally, LaCoO$_3$(RG) was dried at 200 °C under air for 2 h. No subsequent calcination step in air at 600 °C was achieved on this solid.

2.2. Physicochemical characterization

X-ray diffraction (XRD) patterns were recorded on a HUBER G-670 diffractometer equipped with a Cu Kα (λ = 0.154 nm) radiation. Bulk composition of the solid was obtained by X-ray fluorescence analysis on Horiba XGT-7000 apparatus using a Rhodium source. Transmission electron microscopy (TEM) and energy dispersive X-ray analysis (EDX) were collected on a JEOL JEM 2010 microscope operating at 200 kV equipped with a PGT Imix PC system. XPS experiments were performed using a Vacuum Generators Escalab 220XL spectrometer equipped with a mono-chromatized aluminium source for excitation in the analysis chamber under ultra high vacuum ($\sim$10^{-10} Torr). Binding energy (B.E.) values were referenced to the binding energy of the C 1s core level (285.1 eV). The relative quantification was achieved using a mixed Gaussian/Lorentzian peak fit keeping binding energies and half-widths constant for all spectral decomposition. H$_2$-temperature-programmed reduction experiments (H$_2$-TPR) were carried out in a Micromeritics Autochem II 2920 with 5 vol.% H$_2$ in Ar and a gradual heating rate of 5 °C/min. Temperature-programmed desorption experiments (TPD) were carried out in the same device under He flowing at 10 °C/min. The outlet gas mixture was

simultaneously analyzed using a GEV 010 Omnistar mass spectrometer.

2.3. Catalytic measurements

Temperature-programmed reaction experiments (TPR) were performed at atmospheric pressure in a fixed bed flow reactor containing 0.7 g of catalyst exposed to a reaction mixture composed of 0.1 vol.% N$_2$O, 0.1 vol.% NO, 3 vol.% O$_2$ and 0.5 vol.% H$_2$O with He as carrier gas. The global flow rate was 15 L/h corresponding to a gas hourly space velocity of approximately 10,000 h^{-1}. Before reaction, all catalyst samples were pre-heated in He at 500 °C for 1 h. After cooling down and stabilization at 25 °C, the reactant mixture was introduced and the temperature was gradually increased at a controlled heating rate of 3 °C/min. The outlet gas mixture was analyzed with a µGC VARIAN 4900 chromatograph fitted with two thermal conductivity detectors. Prior detection and quantification, NO, O$_2$, N$_2$O and N$_2$ were separated on two parallel 5 Å molecular sieve and poraplot Q columns. NO$_2$ was analyzed by a GEV 010 Omnistar mass spectrometer.

The conversion of N$_2$O (X_{N_2O}) leading to the production of N$_2$ and O$_2$ was calculated according to Eq. (1) where $F^0_{N_2O}$ and F_{N_2O} are respectively the inlet and outlet molar flow rate of N$_2$O.

$$X_{N_2O} = \frac{F^0_{N_2O} - F_{N_2O}}{F^0_{N_2O}} \tag{1}$$

The specific rate r_i related to the conversion of the compound i was calculated according to Eq. (2) with i = N$_2$O or NO. m stands for the mass of catalyst.

$$r_i = \frac{F^0_i X_i}{m} \tag{2}$$

3. Results and discussion

3.1. Influence of the preparation method on the surface and bulk properties of LaCoO$_3$

Specific surface areas of LaCoO$_3$ collected in Table 1 show that the reactive grinding method leads to the highest value of 50 m^2/g which approximately corresponds to the order of magnitude previously reported on LaCoO$_3$ using this method [28]. By contrast, the solid obtained from the template method exhibits an unexpected low value of 12 m^2/g. XRD patterns in Fig. 1 exhibit the typical X-ray lines of the rhombohedral structure of LaCoO$_3$ irrespective of the preparation method. No bulk impurity such as Co$_3$O$_4$ and La$_2$O$_3$ is detectable. As observed, a shift of the X-ray lines towards lower 2θ values occurs on LaCoO$_3$(RG). The crystallite size has been estimated according to the usual Scherrer equation. Calculations, summarized in Table 1, show an increase of the crystallite size within the sequence: RG < SG < T which seems to be in rather good agreement with changes of the specific surface area. The smallest crystallite size on LaCoO$_3$(RG) was expected because particle sintering does not significantly occur during the drying step at moderate temperature (200 °C) [28] contrarily to

Table 1
Textural and structural properties of LaCoO$_3$ according to the preparation method.

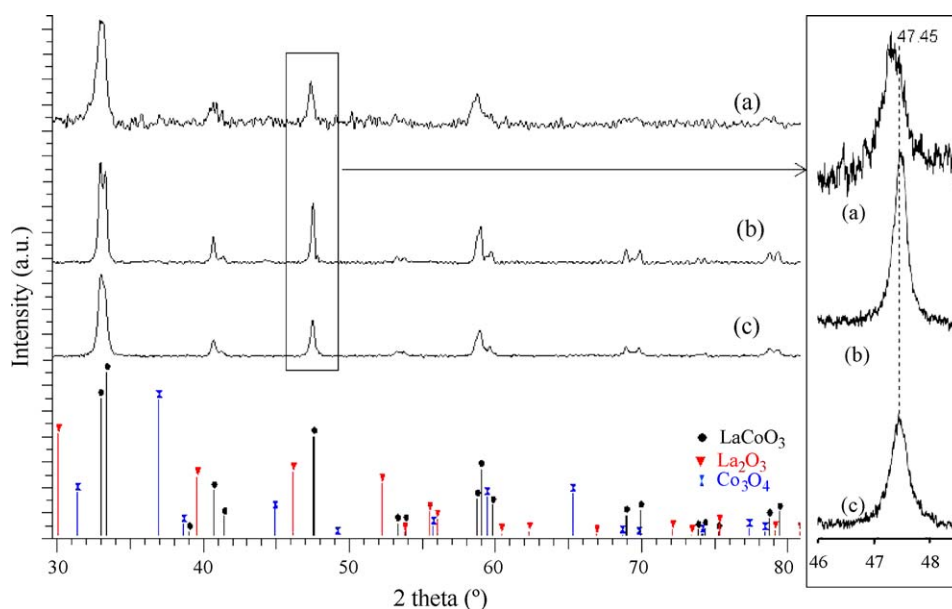| Catalyst	Specific surf. area (m^2/g)	Crystallite size (nm)		
		BET	XRD	TEM
LaCoO$_3$(T)	12	69	30	25
LaCoO$_3$(SG)	20	41	20	29
LaCoO$_3$(RG)	50	16	13.5	17

Fig. 1. Ex situ XRD analysis of freshly prepared $LaCoO_3$ samples: (a) $LaCoO_3(RG)$; (b) $LaCoO_3(T)$; (c) $LaCoO_3(SG)$.

$LaCoO_3(SG)$ and $LaCoO_3(T)$ calcined in air at 600 °C. More surprising is the observation of larger crystallites on $LaCoO_3(T)$ than on $LaCoO_3(SG)$ in comparison with earlier investigations on $LaFeO_3$ using alkoxy-method in the presence and in the absence of the polystyrene spheres as template [22]. In fact, those authors do not observed significant changes on the structural properties, i.e. on the crystallite size. Additional results using the porosity of silica xerogel lead to significant structural changes according to the type of structure and the nature of the cation incorporated inside the structure [21]. As explained, the template was made up of mesopores in the 2–15 nm range which lead to the conclusion that the porosity of the template, as well as the nature of the elements, can strongly influence the structural and textural properties of the resulting materials. Let us mention that the average diameter size of the polystyrene spheres used in this study is substantially higher that earlier reported by Sadakane et al. [22] (400 nm vs. 161 nm). Consequently, the unexpected high crystallite size obtained on $LaCoO_3(T)$ could be partly explained by the high diameter of the polystyrene spheres used in the synthesis. X-ray fluorescence analysis also reveals on $LaCoO_3(RG)$ the presence of iron and zinc impurities (see Table 2). Such a contamination previously reported [28] is inherent to the synthesis method due to an incomplete leaching process and to the milling performed with steel balls in a steel vial [28]. Interestingly, no bulk detectable FeO_x species is observed from XRD analysis despite a significant iron contamination which would suggest that the amount of extra framework Fe contaminant would be much lower than that incorporated into the crystal lattice. Such an explanation is supported by the shift of X-ray lines toward lower value as previously found [29] when iron is incorporated in the perovskite

structure during the synthesis route. TEM measurements confirmed XRD observations regarding the evolution of the crystallite size (see Table 1). As exemplified in Fig. 2(a)–(c), $LaCoO_3$ appears as dense materials with comparable average particle size on $LaCoO_3(SG)$ (29 nm vs. 20 nm from XRD analysis). A broadening of particles size distribution is noticeable on $LaCoO_3(T)$ in the range 2–60 nm (Fig. 3). Finally, TEM images recorded on $LaCoO_3(RG)$ underline the presence of smaller particles with an average size of 17 nm and a narrower particle size distribution. EDX analysis provides complementary information. Nine spots were recorded on each $LaCoO_3$ sample, corresponding to different areas, in order to check the composition homogeneity. EDX spectra corresponding to one spot analysis of $LaCoO_3$ are collected in Fig. 4. Particular attention has been paid to the intensity signals assigned to Co and La. The characterization of Fe and Zn corroborates previous XRD observations. Fig. 5 summarized EDX data collected on the different patterns by examining changes in the relative La/Co intensity ratio (I_{La}/I_{Co}). As observed, only slight variations are distinguishable on I_{La}/I_{Co} (proportional to the atomic ratio) in the range 0.7–0.9 and 0.6–0.7 respectively on $LaCoO_3(SG)$ and $LaCoO_3(RG)$ which leads to the conclusion that La and Co are homogeneously distributed in the solid. On the other hand, the amplitude of variations of I_{La}/I_{Co} on $LaCoO_3(T)$ drastically increases from 0 to $\approx$9.2 which underlines a strong heterogeneity in connexion with the segregation of Co_3O_4 or La_2O_3 phases, respectively.

Surface composition has been analyzed by XPS, Co 2p spectra are collected in Fig. 6. The binding energy value of Co $2p_{3/2}$ photopeak at 780 eV is characteristic of Co^{3+} with the typical shake-up structure at 789.5 eV. However, the presence of small

Table 2
Semi-quantitative XPS and XRF analysis of $LaCoO_3$.

Catalysts	Surface atomic ratio[a]					
	Co/La	C/La[b]	C/La[c]	O/La	Fe/La	Zn/La
$LaCoO_3(T)$	0.40 (1.02)	2.08	0.37	2.84	–	–
$LaCoO_3(SG)$	0.62 (1.01)	0.91	0.54	3.65	–	–
$LaCoO_3(RG)$	0.70 (0.91)	1.51	0.58	4.39 (2.7)	0.10 (0.11)	0.07 (0.12)

[a] (In brackets) Bulk composition from XRF measurements.
[b] Calculated from the total contribution of the C 1s photopeak.
[c] Calculated from the 289.4 eV contribution of the C 1s photopeak related to carbonate species.
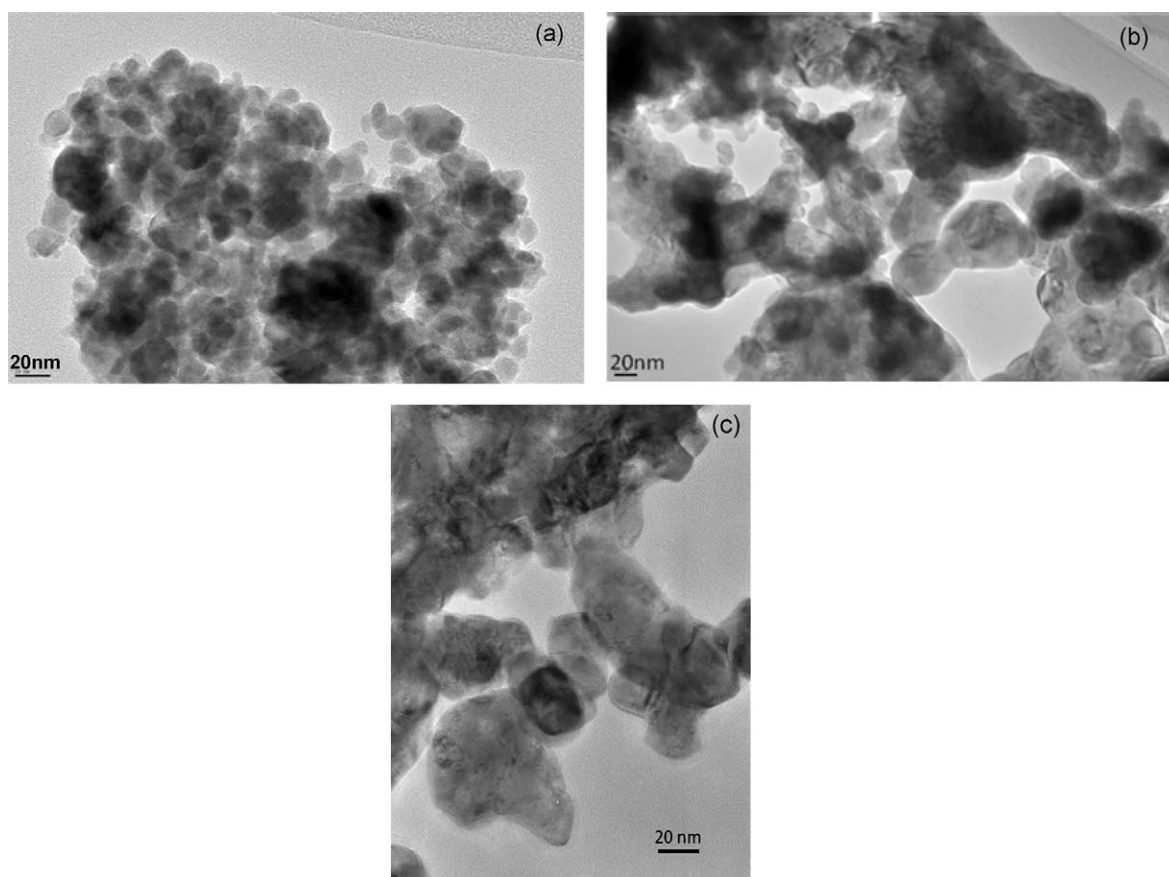
Fig. 2. Transmission electronic microscopy images on $LaCoO_3$: (a) $LaCoO_3$(RG); (b) $LaCoO_3$(T); (c) $LaCoO_3$(SG).

amount of Co^{2+} cannot be completely ruled out on $LaCoO_3$(RG) and $LaCoO_3$(T) with the appearance of a weak contribution at 785.6 eV corresponding to the shake-up structure of Co^{2+} in agreement with previous assignments [30]. Kaliaguine et al. [28] also observed the formation of Co^{2+} on $LaCoO_3$ prepared by reactive grinding with an enhancement of the concentration of Co^{2+} with a rise in the calcination temperature. The O 1s photopeak in Fig. 6 exhibits a contribution at 531.3 eV assigned to hydroxyl groups, O^- or O_2^-

species adsorbed at the surface whereas the low B.E. contribution is usually assigned to lattice oxygen O^{2-} from $LaCoO_3$ [28,31]. In accordance with previous investigations [28], the relative intensity of the contribution at 531.3 eV significantly increases on $LaCoO_3$(RG) which seems to be consistent with the highest specific surface area obtained after calcination at significant lower temperature (200 °C). The examination of the C 1s photopeak in Fig. 6 also reveals the presence of carbonates species characterized
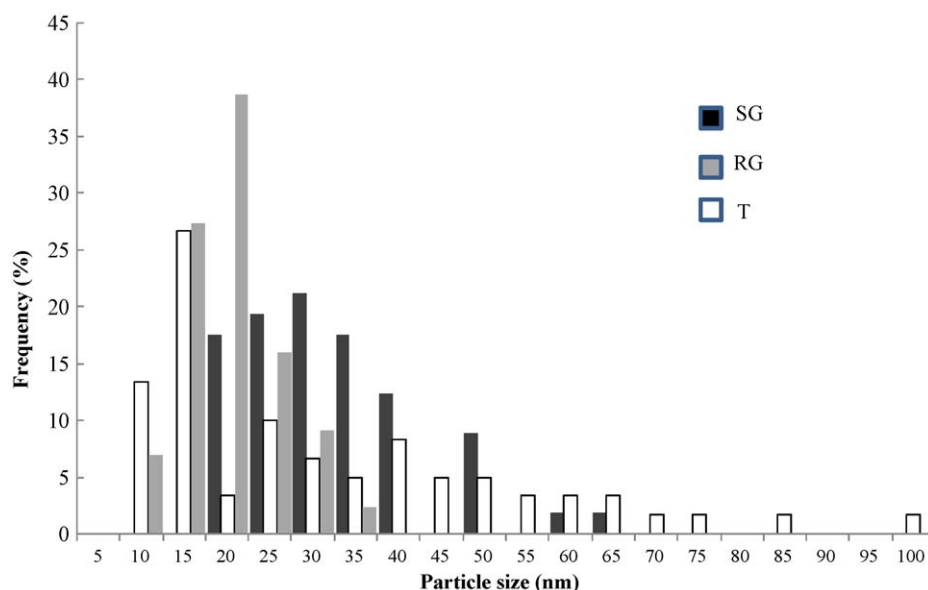

Fig. 3. Distribution of particle size obtained from TEM measurements on $LaCoO_3$(RG), $LaCoO_3$(T) and $LaCoO_3$(SG).
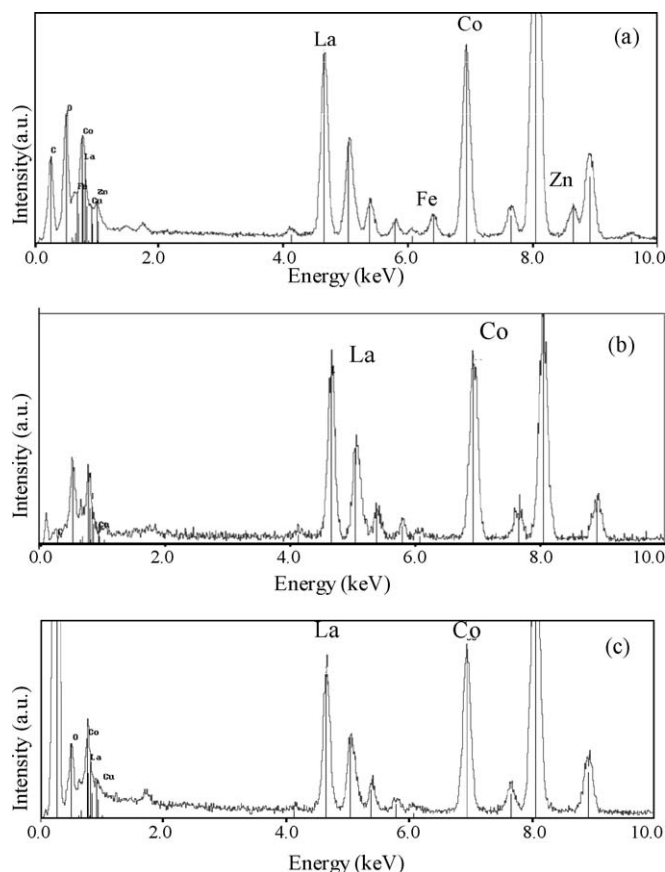
Fig. 4. Local energy-dispersive X-ray analysis on LaCoO₃: (a) LaCoO₃(RG); (a) LaCoO₃(T); (c) LaCoO₃(SG).

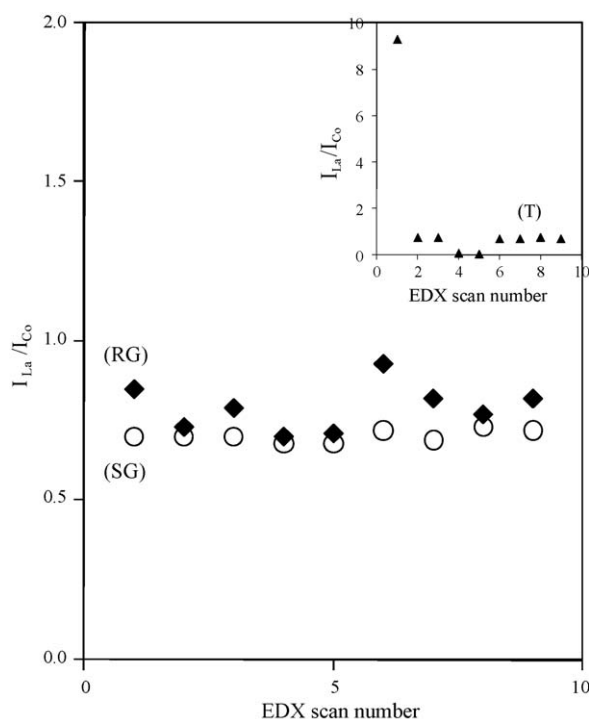**Fig. 5.** La/Co intensity ratios obtained by energy-dispersive X-ray analysis corresponding to nine spots: (◆) LaCoO₃(RG); (▲) LaCoO₃(T); (○) LaCoO₃(SG).

at 289.4 eV. As observed, more extensive formation of these species, after storage in air, takes place on LaCoO₃(RG). According to the above-mentioned observations the surface concentration of these chemisorbed carbon-containing species (Table 2) can be compared to the specific surface area in Table 1. Higher amount of carbonate is associated with the higher specific surface area and probably higher oxygen mobility. XPS data collected in Table 2 confirm the presence of zinc and iron at the surface with small contributions located at 1021.2 and 711.2 eV (see Fig. 7) ascribed to Zn^{2+} and Fe^{3+} [30]. Interestingly, comparable values for the atomic Fe/La ratio have been obtained from XPS and XRF analysis. The depth analyzed by XPS represents approximately 50–100 Å vs. 10 μm for XRF. Hence, it seems obvious that surface and bulk compositions provided by both techniques exhibit the same composition which emphasizes the fact that Fe is more probably homogeneously distributed in the solid rather than segregated at the surface.

3.2. Surface and bulk mobility and reactivity of oxygen from LaCoO₃

Subsequent bulk characterizations were performed in order to investigate the mobility and the reactivity of oxygen species from the perovskite. Tentative correlations with XPS data were achieved on the basis of the spectral features earlier described in Fig. 6 regarding the O 1s and C 1s core levels.

Fig. 8 illustrates H_2 consumption profiles vs. temperature recorded during H_2-TPR experiments on LaCoO₃. As observed, two H_2 consumption ranges highlight a two-step reduction process earlier discussed [4]. Subsequent calculations of the atomic H/Co ratio emphasize the fact that Co^{3+} reduces to Co^{2+} at low temperature whereas the complete reduction of Co^{2+} to metallic Co species takes place at high temperature above 450 °C. Interestingly, LaCoO₃(T) reduces at much higher temperature than LaCoO₃(SG) and LaCoO₃(RG) which could partly be explained by the formation of larger and likely less reducible crystallites and also the stabilization of bulk Co oxides impurities as evidenced from EDX analysis. Intriguingly, LaCoO₃(RG), characterized by smaller crystallites, reduces at higher temperature than LaCoO₃(SG). As observed, the two-step reduction process is delayed with slightly lower value for the atomic H/Co ratio. Such behavior could be induced by iron incorporation in the crystal lattice of the perovskite lowering its reducibility as previously found [29].

Additional TPD-MS analysis was performed in order to investigate the oxygen release. Numerous investigations have already assigned different oxygen species from the desorption of O-containing species at the surface and oxygen lattice [10,14,15,24,28]. However, some of them are incomplete with sometimes controversial assignments in the absence of detailed information on the composition of the outlet gas regarding the occurrence of extra CO_2 desorption. Additionally, only a few of them reported relevant correlations with XPS features which may support assignments from TPD measurements [15,24,28]. Temperature-programmed desorption experiments were performed on the solids in situ pre-activated under 5 vol.% O_2 diluted in He at 500 °C. O_2-TPD curves are reported in Fig. 9(a). Simultaneous mass spectrometry measurements were performed in order to investigate the outlet gas composition. Particular attention has been paid to CO_2 and O_2 formation connected to the MS signals at m/z = 44 and 32, respectively. At low temperature, weak and broad TCD and MS signals appear on LaCoO₃(T) above 450 °C corresponding to O_2 desorption. An intense TCD signal predominates above 650 °C correlated to significant deviation of the m/z = 32 signal (Fig. 9(a) and (b)) associated to a predominant oxygen desorption. Let us observe in Fig. 9(c) the presence of a weak and broad signal above 650 °C related to a low CO_2 detection likely due to the
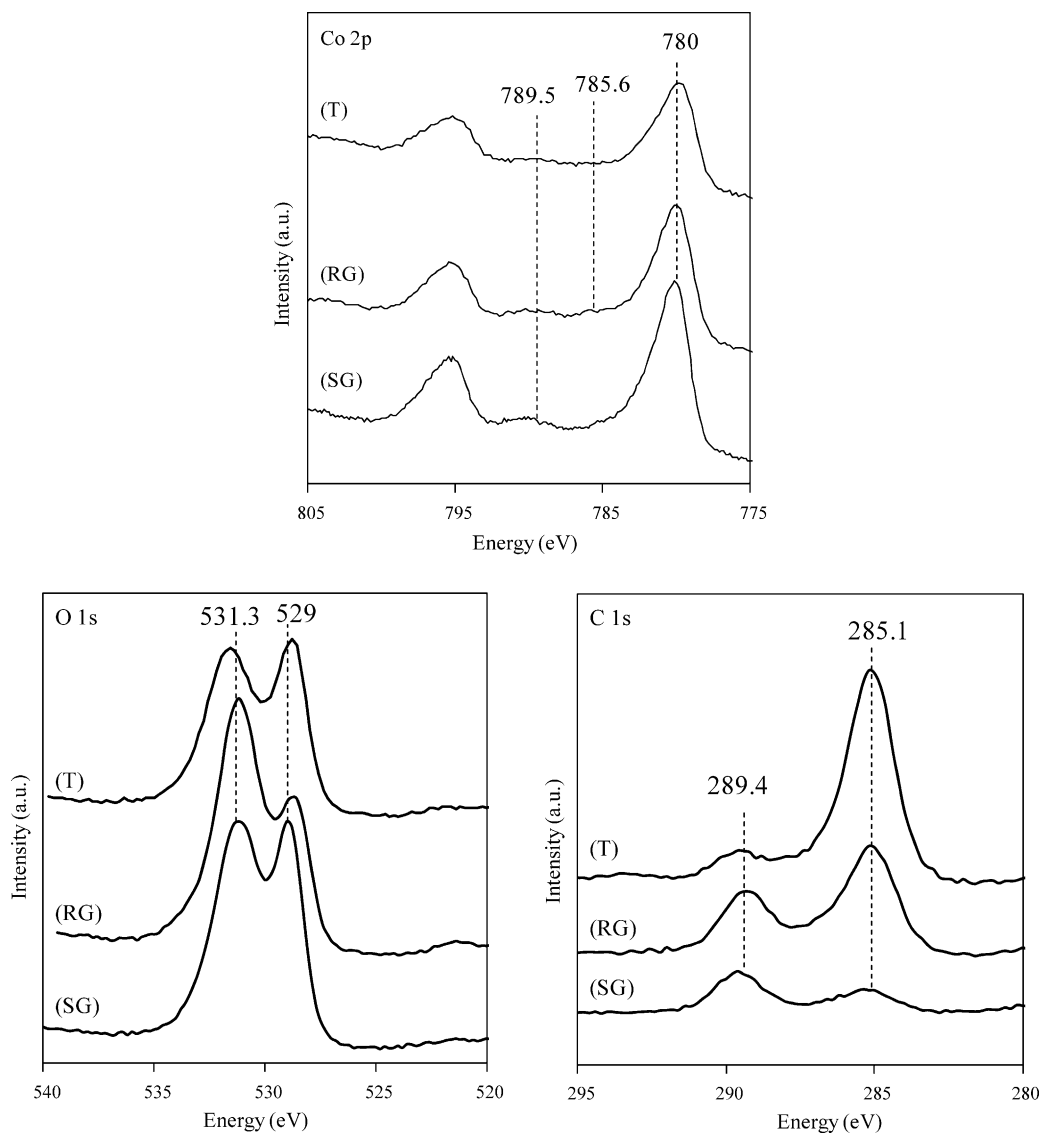
Fig. 6. XPS analysis on LaCoO₃: Co 2p, O 1s and C1s spectra recorded on LaCoO₃.
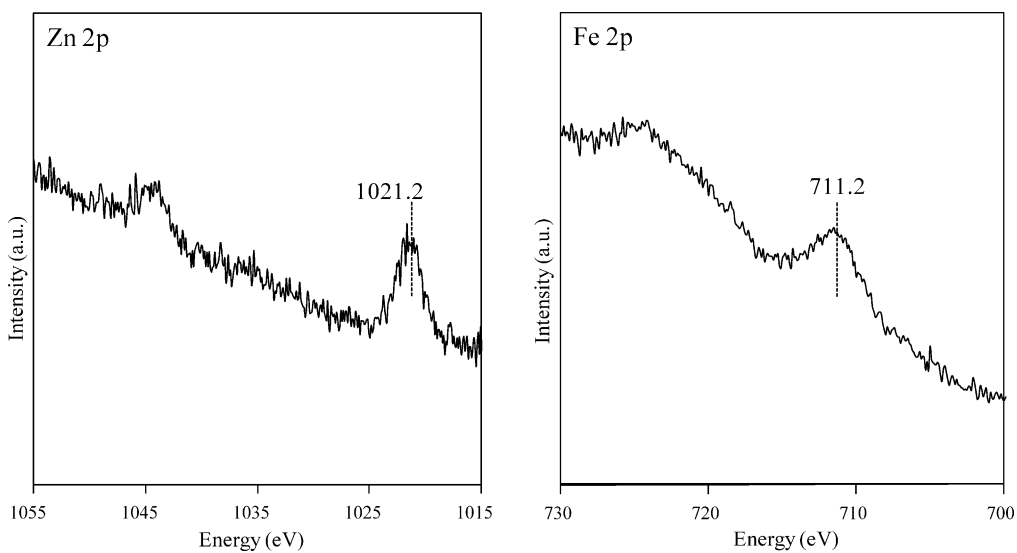
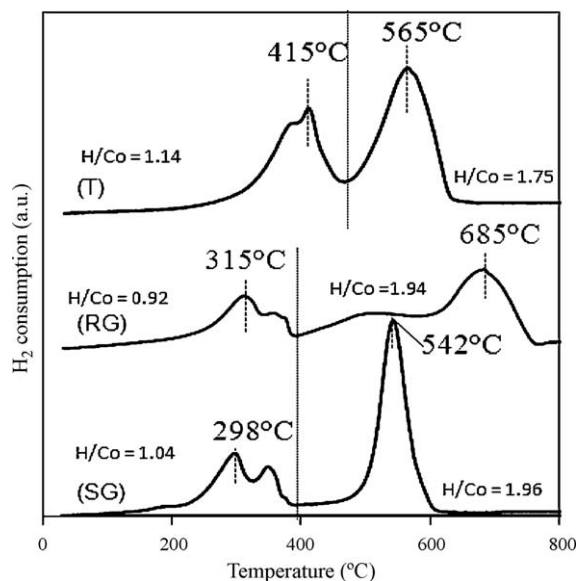**Fig. 7.** XPS analysis on LaCoO₃(RG) sample: Fe 2p and Zn 2p spectra.

Fig. 8. H_2-temperature-programmed reduction under 5% H_2/Ar on $LaCoO_3(T)$, $LaCoO_3(RG)$ and $LaCoO_3(SG)$ and H/Co atomic ratio.
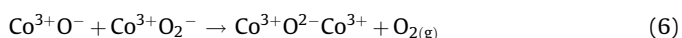
decomposition of carbonates. The low temperature processes ($T > 480$ °C), which are usually referred to α-O_2 desorption [10,15], intensify on $LaCoO_3(RG)$. It has been earlier discussed and currently ascribed to the desorption of OH, O^- and/or O_2^- species weakly bound to the surface of $LaCoO_3$ leading to the formation of anionic vacancies according to step (3) [15]. This desorption process can be easily correlated to the sharp increase in the high B.E. contribution on the O 1s photopeak recorded on $LaCoO_3(RG)$ (see Fig. 6). The intense and narrower desorption peak at $\cong 930$ °C (β-O_2 peak) corresponds to the desorption of lattice oxygen O^{2-}. It is worthwhile to note that the desorption of CO_2 ($m/z = 44$) occurs more readily and more extensively on $LaCoO_3(RG)$ than on $LaCoO_3(T)$ and $LaCoO_3(SG)$ which agrees with previous XPS observations associated to the relative contribution of the 289.4 eV photopeak on the atomic C/La ratio. Finally, it is worthwhile to note that weak α and β oxygen desorption process seems to occur on $LaCoO_3(SG)$ in the temperature range of the study. Such an observation can be explained on the basis of previous findings reported by Kaliaguine et al. [28] who earlier described the elementary processes associated to both oxygen formation processes involving different transient surface species. They suggested a two-step dehydroxylation process according to steps (3) and (4):

$$2Co^{3+}(OH)^- \rightarrow Co^{3+}O^- + Co^{2+}V_o + H_2O \tag{3}$$

$$Co^{3+}O^- + Co^{2+}V_o \rightarrow Co^{3+}O^{2-}Co^{3+} \tag{4}$$
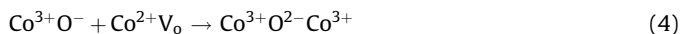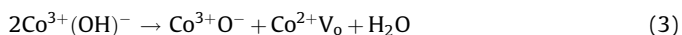
Subsequent interactions between anionic vacancies and oxygen in the gas phase may originate step (5):

$$Co^{2+}V_o + O_2 \rightarrow Co^{3+}O_2^- \tag{5}$$

Finally, α-O_2 desorption according to steps (6) and (7) may take place.

$$Co^{3+}O^- + Co^{3+}O_2^- \rightarrow Co^{3+}O^{2-}Co^{3+} + O_{2(g)} \tag{6}$$

or

$$Co^{3+}O_2^- \rightarrow Co^{2+} + O_{2(g)} \tag{7}$$

Previous explanations reported elsewhere [28] are consistent with our proper observations on $LaCoO_3(RG)$ and $LaCoO_3(T)$. As a matter of fact, the involvement of step (7) during an increase in
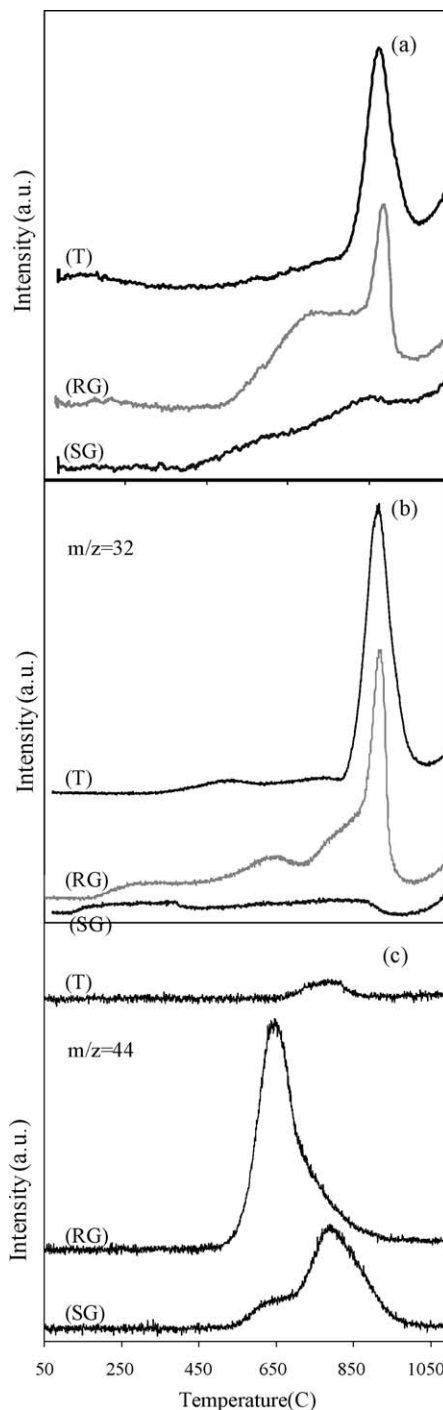

Fig. 9. Temperature-programmed desorption under Helium on $LaCoO_3(T)$, $LaCoO_3(RG)$ and $LaCoO_3(SG)$. Simultaneous TCD (a) and MS on-line detection with $m/z = 32$ (b) and 44 (c) assigned to O_2 and CO_2 in the gas phase.

calcination temperature and/or during thermal desorption of oxygen would lead to an enhancement of the concentration of Co^{2+}, as indicated by XPS (see Fig. 6). Consistently, the absence of significant desorption on $LaCoO_3(SG)$ seems to be well in agreement with the preferential observation of Co^{3+} as seen in Fig. 6.

3.3. Catalytic performances of $LaCoO_3$ in the decomposition of N_2O

The catalytic activity of $LaCoO_3$ prepared by these different methods was evaluated in the decomposition of N_2O in the presence of NO, water and excess O_2. As indicated in the
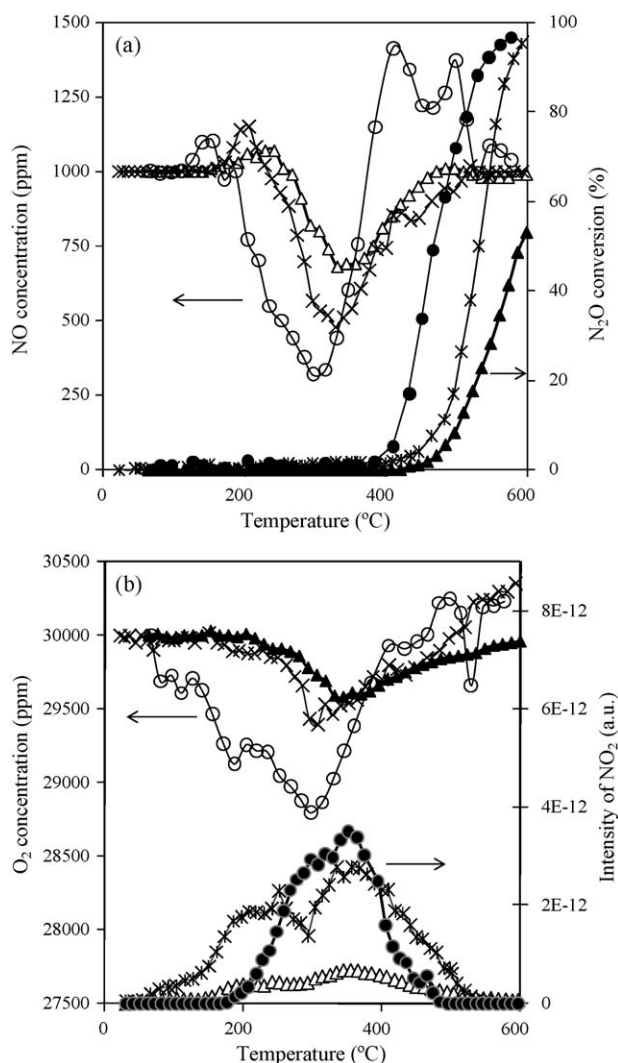
Fig. 10. N_2O conversion and NO concentration profiles vs. temperature (a); O_2 concentration and NO_2 MS signal vs. temperature (b) on $LaCoO_3(T)$ (▲, △), $LaCoO_3(RG)$ (●, ○) and $LaCoO_3(SG)$ (*, ×) recorded during temperature-programmed experiments in the presence of 0.1 vol.% N_2O, 0.1 vol.% NO, 3 vol.% O_2 and 0.5 vol.% H_2O.

experimental section, catalyst samples were pre-heated in He at 500 °C before reaction. Temperature-programmed conversion curves of N_2O vs. temperature are reported in Fig. 10(a). The evolution of the NO concentration has been simultaneously recorded and correlated to O_2 consumption and NO_2 formation in Fig. 10(b). All these information emphasize the fact that complex catalytic features characterise $LaCoO_3$ with the occurrence of parallel and successive reactions. Two major observations are related to the conversion of NO essentially to NO_2 at low temperature whereas the catalytic decomposition of N_2O takes place above 400 °C. The overall activity can be qualitatively estimated on the basis of the light-off temperature, T_{50}, corresponding to 50% N_2O conversion. The following activity sequence can be established: $LaCoO_3(RG)$ $T_{50} = 467$ °C > $LaCoO_3(SG)$ $T_{50} = 531$ °C > $LaCoO_3(T)$ $T_{50} = 590$ °C which highlights the best catalytic performances of $LaCoO_3(RG)$. More careful description leads to additional comments particularly on $LaCoO_3(RG)$. As observed, the conversion curve of NO correlated to the formation of NO_2 does not coincide to the consumption profile of oxygen which starts at lower temperature (63 °C vs. 188 °C for the conversion of NO to NO_2). Such a feature corroborates previous O_2-TPD and XPS observations on

$LaCoO_3(RG)$ showing a significant O_2 desorption above 450 °C and a greater stabilization of Co^{2+} from XPS measurements. Consequently, O_2 adsorption via step (5) would essentially proceed on pre-activated $LaCoO_3(RG)$ in the temperature range 63–188 °C. Subsequent increase in temperature leads to the formation of gaseous NO_2 and probably to the subsequent formation of chemisorbed ad-NO_x species (nitrites/nitrates). An extra NO and O_2 formation above 400 °C supports the formation of nitrates species which decompose at that temperature on $LaCoO_3(RG)$. As observed no significant extra NO formation is discernible on $LaCoO_3(T)$ and $LaCoO_3(SG)$.

3.4. Tentative correlations between physicochemical and catalytic properties

As observed, $LaCoO_3$ exhibits two different catalytic behaviors associated with the oxidation of NO to NO_2 in the temperature range 200–450 °C, and the decomposition of N_2O starting at higher temperature. It is interesting to note that no decomposition of NO occurs in the temperature range of this study. As exemplified in Fig. 10, $LaCoO_3(RG)$ produces NO_2 and decomposes N_2O more readily than $LaCoO_3(T)$ and $LaCoO_3(SG)$. Specific and intrinsic rates for both reactions have been roughly calculated on the basis of transient NO and N_2O conversion values obtained at 270 and 467 °C, respectively. The results collected in Table 3 show that the best activity of $LaCoO_3(RG)$ for both reactions is not only related to the number of accessible sites at the surface, i.e. to the specific surface area but also to the nature of the sites intrinsically more active than those characterizing $LaCoO_3(T)$ and $LaCoO_3(SG)$. Consistently, the extent of interactions between adsorbates and the surface of $LaCoO_3$ should be altered according to the preparation method. O_2-TPD and TPR experiments provide interesting information. As suggested in Fig. 9, stable carbonates would not be completely removed after the pre-activation of $LaCoO_3(T)$ and $LaCoO_3(SG)$ in He at 500 °C, whereas the release of CO_2 observed at lower temperature on $LaCoO_3(RG)$ with successive α-O_2 desorption would provide anionic vacancies potentially active for the adsorption and the decomposition of N_2O. Let us notice that the α-O_2 desorption is delayed on $LaCoO_3(T)$ and $LaCoO_3(SG)$ which agrees with the loss of activity in the decomposition of N_2O. Such an explanation seems to be in line with previous conclusions [10] indicating that a weaker adsorption of oxygen can be related to a larger mobility of oxygen and a higher activity for NO decomposition. Hence, the extent of N_2O decomposition is likely correlated to the presence of defect structures as reported elsewhere [18].

Now, returning to the temperature-programmed experiments, the examination of the peculiar catalytic properties of $LaCoO_3(RG)$ for the catalytic oxidation of NO and the decomposition of N_2O can be explained on the basis of steps (3)–(7) and the occurrence of competitive reactions leading to the formation of nitrates. As earlier reported the presence of nitrates may also originate strong inhibiting effects in the rate of N_2O decomposition. Hence, at low temperature, it has been found that the competition between O_2 and

Table 3
Influence of the preparation method of $LaCoO_3$ on the catalytic performances.

Catalysts	NO oxidation to NO_2[a]		N_2O decomposition[b]	
	Specific rate[c]	Intrinsic rate[d]	Specific rate[c]	Intrinsic rate[d]
$LaCoO_3(T)$	0.10	0.8	0.10	0.8
$LaCoO_3(SG)$	0.54	2.7	0.25	1.25
$LaCoO_3(RG)$	1.76	3.5	1.56	3.1

[a] From TPR experiments at $T = 270$ °C.
[b] From TPR experiments at $T = 467$ °C.
[c] mol s^{-1} g^{-1}.
[d] $\times 10^{-2}$ mol s^{-1} m^{-2}.

NO on $Co^{2+}V_o$, generated during the pre-activation thermal treatment, is in favor of O_2 according to step (5). Such a competition suppresses the catalytic decomposition of NO and N_2O into nitrogen. Subsequent reactions, between surface O_2^- species and NO probably lead to the formation of ad-NO_x species. As indicated in Table 3, NO_2 formation would occur more readily on $LaCoO_3(RG)$ than on $LaCoO_3(T)$ and $LaCoO_3(SG)$ based on the comparison of the intrinsic rate values. Nevertheless, nitrates species weakly interact on $LaCoO_3(RG)$ and decompose at lower temperature than on $LaCoO_3(T)$ and $LaCoO_3(SG)$ with parallel desorption of oxygen activated in this temperature range according to steps (6) and (7). Consequently, the restoration of anionic vacancies $Co^{2+}V_o$ at lower temperature could partly explain the higher activity of $LaCoO_3(RG)$ in the decomposition of N_2O on $LaCoO_3(RG)$. Such an explanation is consistent with physicochemical characterization. XPS, XRD, EDX and H_2-TPR observations show that iron impurities on $LaCoO_3(RG)$ are likely incorporated inside the crystal lattice of $LaCoO_3$. Previous investigations reported subsequent expansion of the unit cell due to a partial Fe incorporation in $LaCoO_3$ inducing a weakening of the Co–O bond [29]. Such a phenomenon is probably a key factor in determining the catalytic performances with a higher concentration of anionic vacancies on $LaCoO_3(RG)$ potentially active for the decomposition of N_2O.

4. Conclusion

In conclusion, the present study showed that the preparation method of $LaCoO_3$ perovskites influences the catalytic activity of N_2O decomposition. Results showed that morphology and surface changes may induce strong differences in the catalytic activity of $LaCoO_3$ in N_2O decomposition even if they are characterized by the same rhombohedral structure. $LaCoO_3$ prepared by the reactive grinding method exhibits the highest activity for the catalytic decomposition of N_2O. This was related to higher specific area and higher density of oxygen vacancies. As a matter of fact, results obtained also indicate that the overall activity is closely related to the mobility of oxygen species with different extent of interactions between carbonates and nitrates. It has been concluded that the partial incorporation of iron impurities during the preparation of $LaCoO_3(RG)$ governs the catalytic performances towards the decomposition of N_2O.

References

[1] M.N. Debbagh, C. Salinas Martinez de Lecea, J. Pérez-Ramírez, Appl. Catal. B 70 (2007) 335.
[2] P. Granger, P. Esteves, S. Kieger, L. Navascues, G. Leclercq, Appl. Catal. B 62 (2006) 236.
[3] G. Centi, L. Dall'Olio, S. Perathoner, J. Catal. 192 (2000) 224.
[4] J.P. Dacquin, C. Dujardin, P. Granger, J. Catal. 253 (2008) 37.
[5] G. Delahay, M. Mauvezin, B. Coq, S. Kieger, J. Catal. 202 (2001) 156.
[6] J. Pérez-Ramírez, Appl. Catal. B 70 (2007) 31.
[7] J. Pérez-Ramírez, F. Kapteijn, K. Schöffel, J.A. Moulijn, Appl. Catal. B 44 (2003) 117.
[8] M.A. Peña, J.L. Fierro, Chem. Rev. 101 (2001) 1981.
[9] J. Zhu, D. Xiao, J. Li, X. Xie, X. Yiang, Y. Wu, J. Mol. Catal. A 233 (2005) 29.
[10] Z. Zhao, X. Yang, Y. Wu, Appl. Catal. B 8 (1996) 281.
[11] F. Kapteijn, J. Rodrigues-Mirasol, J.A. Moulijn, Appl. Catal. B 9 (1996) 25.
[12] Y. Zhu, D. Wang, F. Yuan, G. Zhang, H. Fu, Appl. Catal. B 82 (2008) 255.
[13] H. Iwakuni, Y. Shinmyou, H. Yano, H. Matsumoto, T. Ishihara, Appl. Catal. B 74 (2007) 299.
[14] H. He, H.X. Dai, C.T. Au, Appl. Catal. B 33 (2001) 65.
[15] G.L. Chiarello, D. Ferri, J.D. Grundwaldt, L. Forni, A. Baiker, J. Catal. 252 (2007) 137.
[16] C.N. Costa, V.N. Stathopoulos, V.C. Belessi, A.M. Efstathiou, J. Catal. 197 (2001) 350.
[17] D. Ferri, L. Forni, M.A.P. Dekkers, B.E. Nieuwenhuys, Appl. Catal. B 16 (1998) 339.
[18] C. Tofan, D. Klvana, J. Kirchnerova, Appl. Catal. B 36 (2002) 311.
[19] T. Ishihara, M. Ando, K. Sada, K. Takiishi, K. Yamada, H. Nishiguchi, Y. Takita, J. Catal. 220 (2003) 104.
[20] M. Engelmann-Pirez, P. Granger, G. Leclercq, Catal. Today 107–108 (2005) 315.
[21] T. Valdés-Solis, G. Marbán, A.B. Fuertes, Chem. Mater. 17 (2005) 1919.
[22] M. Sadakane, T. Asanuma, J. Kubo, W. Ueda, Chem. Mater. 17 (13) (2005) 3546.
[23] V. Szabo, M. Bassir, A. Van Neste, S. Kaliaguine, Appl. Catal. B 37 (2002) 175.
[24] R. Zhang, A. Villanueva, H. Alamdari, S. Kaliaguine, Appl. Catal. B 64 (2006) 220.
[25] H. Tagushi, S.I. Matsu-ura, M. Nagao, T. Choso, K. Kabata, J. Solid State Chem. 129 (1997) 60.
[26] M.S.G. Baithoun, F.R. Sale, J. Mater. Sci. 17 (1982) 2757.
[27] S. Vaudreuil, M. Bousmina, S. Kaliaguine, L. Bonneviot, Adv. Mater. 13 (17) (2001) 1310.
[28] S. Kaliaguine, A. Van Neste, V. Szabo, J.E. Gallot, M. Bassir, R. Muzychuk, Appl. Catal. A 209 (2001) 345.
[29] N.A. Merino, B.P. Barbero, P. Ruiz, L.E. Cadús, J. Catal. 240 (2006) 245.
[30] D. Briggs, M.P. Seah, 2nd ed., Practical Surface Analysis, vol. 1, Wiley, New York, 1983, p. 613.
[31] M.M. Natile, E. Ugel, C. Maccato, A. Glisenti, Appl. Catal. B 72 (2007) 351.